Metallurgically lithiated SiO_x anode with high capacity and ambient air compatibility

Jie Zhao[a], Hyun-Wook Lee[a], Jie Sun[a], Kai Yan[a], Yayuan Liu[a], Wei Liu[a], Zhenda Lu[a], Dingchang Lin[a], Guangmin Zhou[a], and Yi Cui[a,b,1]

[a]Department of Materials Science and Engineering, Stanford University, Stanford, CA 94305; and [b]Stanford Institute for Materials and Energy Sciences, SLAC National Accelerator Laboratory, Menlo Park, CA 94025

Edited by Thomas E. Mallouk, The Pennsylvania State University, University Park, PA, and approved May 10, 2016 (received for review March 7, 2016)

A common issue plaguing battery anodes is the large consumption of lithium in the initial cycle as a result of the formation of a solid electrolyte interphase followed by gradual loss in subsequent cycles. It presents a need for prelithiation to compensate for the loss. However, anode prelithiation faces the challenge of high chemical reactivity because of the low anode potential. Previous efforts have produced prelithiated Si nanoparticles with dry air stability, which cannot be stabilized under ambient air. Here, we developed a one-pot metallurgical process to synthesize Li_xSi/Li_2O composites by using low-cost SiO or SiO_2 as the starting material. The resulting composites consist of homogeneously dispersed Li_xSi nanodomains embedded in a highly crystalline Li_2O matrix, providing the composite excellent stability even in ambient air with 40% relative humidity. The composites are readily mixed with various anode materials to achieve high first cycle Coulombic efficiency (CE) of >100% or serve as an excellent anode material by itself with stable cyclability and consistently high CEs (99.81% at the seventh cycle and ∼99.87% for subsequent cycles). Therefore, Li_xSi/Li_2O composites achieved balanced reactivity and stability, promising a significant boost to lithium ion batteries.

prelithiation | silicon oxides | Coulombic efficiency | ambient air compatibility

Lithium ion batteries (LIBs) are vital for portable electronics, electrical transportation, and emerging large-scale stationary energy storage (1, 2). The existing LIBs are produced in the discharged state, in which Li is prestored in cathodes, whereas the anode is free of Li (3, 4). The electrode materials at discharged states are usually air stable and compatible with the manufacturing process. During the first charging cycle, the organic electrolytes are not stable and subjected to decomposition to form a solid electrolyte interphase (SEI) layer on the electrode surface (5, 6). The formation of SEI permanently consumes an appreciable amount of Li to yield low first cycle Coulombic efficiency (CE) (7). The existing graphite has 5–20% first cycle irreversible loss of Li to form SEI, whereas the emerging high-capacity alloy anode, such as Si, Sn, or SiO_x, would have 20–50% loss (8–10). Alloy anodes suffer from the potential mechanical disintegration of the electrode structure and the SEI instability caused by its large volume change during lithiation/delithiation (11, 12). Diverse optimized structural designs, such as nanowires (13–15), porous nanostructures (16, 17), and carbon composite (18, 19), were deployed to address these issues, which yielded improved cycling performance over thousands of cycles. However, advanced nanostructures increase the electrode–electrolyte contact area and thus, exacerbate the irreversible loss of Li (20, 21). Low first cycle CE leads to the consumption of an excess amount of cathode material solely for the first cycle and thereby, significantly reduces the energy density. It is also challenging to effectively compensate for the Li loss through loading excessive cathode materials as a result of kinetic limitations on the cathode thickness (22, 23). Accordingly, there is a strong motivation to develop high-capacity materials to prestore a large amount of Li in either cathode or anode to compensate for the initial loss.

Usually, prelithiation of cathode materials was previously achieved by treating spinel cathode materials or metal oxides with chemical reagents, like *n*-butyllithium, LiI, or molten Li (24–26). However, the prestored capacity is still relatively low (100–800 mAh/g). Li_2S, with a high capacity of 1,166 mAh/g as a cathode material at discharge state, cannot serve as a prelithiation reagent because of the incompatibility of ether electrolytes in Li-S batteries with existing LIB technology (27, 28).

However, anode materials are more attractive Li reservoirs because of the high specific capacities. In previous studies, there have been three main approaches to realize anodes with prestored Li. One approach is electrochemical prelithiation by shorting electrolyte-wetted anodes with Li foil, which requires the fabrication of a temporary cell under inert atmosphere (29, 30). Another approach is to incorporate microscale stabilized lithium metal powder (SLMP; FMC Lithium Corp.) into anodes (31–33). It has been shown that SLMP is effective to compensate for the first cycle Li loss of various anode materials, including graphite and Si. However, synthesis of SLMP in the research laboratory is difficult. Moreover, uniform distribution of SLMP in the anode is still challenging because of the large particle size (34). In our recent report, we showed chemically synthesized Li_xSi nanoparticles (NPs) as an effective prelithiation reagent (35). To enable their stability in dry air and a low-humidity environment, we exposed Li_xSi NPs to trace amounts of dry air, resulting in formation of an Li_2O passivation layer (Fig. 1*A*). We found that the Li_xSi/Li_2O core shell NPs maintained their capacities only in the dry air but that their capacities were reduced drastically after exposure to ambient air. In the follow-up study, we showed that using 1-fluorodecane to modify the surface gives rise to an artificial SEI coating consisting of LiF and Li alkyl

Significance

High-capacity prelithiation of the electrodes is an important strategy to compensate for lithium loss in lithium ion batteries. Because of the high chemical reactivity, conventional prelithiation reagent often presents serious safety concerns. Here, we present a new nanocomposite as the lithium source material with homogeneously dispersed active Li_xSi nanodomains embedded in a robust Li_2O matrix, which exhibits remarkable air compatibility and cycling performance. Other than the potential impact on battery manufacturing, our study focuses on the material science to stabilize active materials by tuning nanostructures and the degree of the crystallinity. Our result is valuable to researchers working with highly sensitive materials and not limited to the batteries community.

Author contributions: J.Z. and Y.C. designed research; J.Z., H.-W.L., J.S., K.Y., Y.L., W.L., Z.L., D.L., and G.Z. performed research; J.Z., H.-W.L., and J.S. contributed new reagents/analytic tools; J.Z., H.-W.L., J.S., Y.L., and Z.L. analyzed data; and J.Z., J.S., K.Y., and Y.C. wrote the paper.

The authors declare no conflict of interest.

This article is a PNAS Direct Submission.

[1]To whom correspondence should be addressed. Email: yicui@stanford.edu.

This article contains supporting information online at www.pnas.org/lookup/suppl/doi:10.1073/pnas.1603810113/-/DCSupplemental.

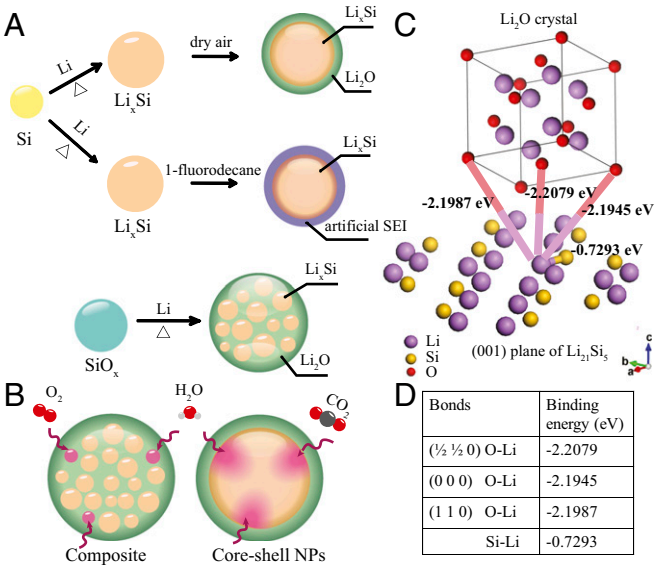

Bonds	Binding energy (eV)
(½ ½ 0) O-Li	-2.2079
(0 0 0) O-Li	-2.1945
(1 1 0) O-Li	-2.1987
Si-Li	-0.7293

Fig. 1. Schematic diagrams and DFT simulation showing the advantages of Li$_x$Si/Li$_2$O composite. (*A*) Three approaches to stabilize reactive Li$_x$Si NPs. (*B*) The different behaviors of Li$_x$Si/Li$_2$O composite and Li$_x$Si/Li$_2$O core shell NPs under the ambient condition. (*C*) DFT simulation is performed by cleaving along the (001) plane of Li$_{21}$Si$_5$ and calculating the binding energy between O at different positions in Li$_2$O and Li at the (001) plane of Li$_{21}$Si$_5$. (*D*) The table shows the binding energy of different bonds.

carbonate with long hydrophobic carbon chains (36). The coated Li$_x$Si NPs showed improved air stability only at a low-humidity level [<10% relative humidity (RH)]. We hypothesize that it is difficult to realize perfect encapsulation and that any pinhole will provide a pathway for inner Li$_x$Si to react with water vapor in the air to significantly reduce the capacity (Fig. 1*B*). Accordingly, an improved strategy for prelithiation has yet to be developed to achieve ambient air compatibility.

In this study, we have successfully shown such a materials strategy. We developed Li$_x$Si/Li$_2$O composites with excellent ambient air compatibility through a one-pot metallurgical process using low-cost SiO or SiO$_2$ as the starting material to alloy thermally with molten Li metal (Fig. 1*A*). The prelithiation capacities of the composites were 2,120 and 1,543 mAh/g based on the masses of SiO and SiO$_2$, respectively. The composite revealed a unique structure with homogeneously dispersed active Li$_x$Si nanodomains embedded in a robust Li$_2$O matrix, which gave the composite an unparalleled stability in both dry air and ambient air conditions. Other than negligible capacity decay in dry air, Li$_x$Si/Li$_2$O composites exhibited a high-capacity retention of 1,240 mAh/g after 6 h of exposure to ambient air (~40% RH). Such superior stability compared with previously developed Li$_x$Si/Li$_2$O core shell NPs (only stable in dry air) is contributed by highly crystalline Li$_2$O matrix formed at high temperature and the enlarged contact area between Li$_2$O and Li$_x$Si as shown in Fig. 1*B*. Thanks to the sufficiently low potential, Li$_x$Si/Li$_2$O composites can be mixed with various anode materials during slurry processing to increase the first cycle CE. In addition, Li$_x$Si/Li$_2$O composite serves as remarkable battery anode material by itself. With stable cycling performance and consistently high CEs (99.81% at the seventh cycle and stable at ~99.87% for subsequent cycles), the composite can potentially replace Li metal anode in the Li-O$_2$ and Li-S batteries (30, 37).

Results and Discussion

Density Functional Theory Simulation. To study the stability of Li$_x$Si NPs in the ambient air condition, we performed density functional theory (DFT) simulation to calculate the interaction between O in Li$_2$O and Li in Li$_{21}$Si$_5$. For simplicity, we cleave along the (001) plane of Li$_{21}$Si$_5$ and calculate the binding energy between O at different positions in Li$_2$O with Li at the center of (001) plane of Li$_{21}$Si$_5$ as shown in Fig. 1*C*. The binding energies between O atoms at (1/2 1/2 0), (100), and (010) positions of Li$_2$O and surface Li are −2.2079, −2.1945, and −2.1987 eV, respectively, much larger than the binding energy between Li and the nearest Si in the (001) plane of Li$_{21}$Si$_5$ with a value of −0.7293 eV. Based on the DFT simulation, enlarging the contact surface between Li$_2$O and Li$_x$Si is necessary. Uniform Li$_x$Si/Li$_2$O composite structure is, therefore, superior to Li$_2$O/Li$_x$Si core shell structure as indicated in Fig. 1*B*. Li$_x$Si/Li$_2$O composite provides more binding between O in Li$_2$O and Li in Li$_{21}$Si$_5$, which effectively stabilizes the Li in Li$_{21}$Si$_5$ nanodomains. There is also an additional factor contributing to the inferior stability of the previous core shell NPs. Namely, it is difficult to realize perfect encapsulation, even with the advanced fabrication process. Any pinhole will provide a pathway for inner Li$_x$Si to react with the air and thus, lose the capacity. In Li$_x$Si/Li$_2$O composite, Li$_x$Si nanodomains are uniformly embedded in a robust Li$_2$O matrix, such that each Li$_x$Si nanodomain has localized Li$_2$O protection. Even if some Li$_x$Si nanodomains are killed because of the presence of pinholes on the surface, the inner Li$_2$O still serves as a localized protection layer to prevent inner Li$_x$Si nanodomains from additional oxidation.

Synthesis and Characterizations of Lithiated SiO NPs. SiO NPs were used as the starting material to form Li$_x$Si/Li$_2$O composite. SiO microparticles (−325 mesh) were first ground to obtain a fine powder by planetary ball milling operated at a grinding speed of 400 rpm (QM-WX04 horizontal type planetary ball mill, Nanjing Nanda Instrument Co., Ltd) for 6 h. Subsequently, the SiO powder was made to react with molten Li, with the color transition from dark red to black immediately on contact. To guarantee uniform lithiation, the mixture of SiO NPs and molten Li (500:509 mg, which is determined by the chemical reaction in Fig. S1*C*) was heated at 250 °C under mechanical stirring inside a tantalum crucible at 200 rpm for at least 1 d in a glove box (Ar atmosphere, O$_2$ level <1.2 ppm, and H$_2$O level <0.1 ppm). Transmission EM (TEM) and SEM were used to characterize the morphology of the SiO NPs before and after lithiation. After ball milling, the size of SiO NPs was in the range of 50–250 nm as shown in Fig. 2*A* and Fig. S1*A*. The size of derived Li$_x$Si/Li$_2$O composite was larger than that of original SiO NPs because of the volume expansion and some degree of particle aggregation during the alloying process (Fig. 2*B* and Fig. S1*B*). To investigate the spatial distribution of various elements, electron energy loss spectroscopy (EELS) mapping was performed on an Li$_x$Si/Li$_2$O particle under the scanning TEM mode. Li signal cannot be detected under the condition of Si and O mapping because of the heavy beam damage through consecutive scans. Therefore, Li element mapping was obtained first at short exposure time followed by Si and O mapping at the same place with longer exposure time per step. Compared with the scanning TEM image, the corresponding EELS elemental mapping reveals that Li, Si, and O elements were uniformly distributed as shown in Fig. 2*C*, indicating the formation of a homogeneous Li$_x$Si/Li$_2$O composite. Furthermore, X-ray diffraction (XRD) confirms the complete transformation of amorphous SiO (Fig. S2) to crystalline Li$_{21}$Si$_5$ [powder diffraction file (PDF) no. 00-018-747] and Li$_2$O (PDF no. 04-001-8930) during the alloying process (Fig. 2*D*). The broad background of the XRD patterns primarily comes from the Kapton tape covering the sample to suppress possible side reactions in the air (Fig. S2). The Li$_x$Si/Li$_2$O composite and the Li$_x$Si/Li$_2$O core shell NPs exhibit different behaviors under TEM electron beam (Fig. 2*E* and Movies S1 and S2). After the core shell NPs were exposed to the electron beam, Li metal started to extend outward, and the whole structure collapsed only after 1 min. EELS spectrum of Li K edge (Fig. S3*B*) confirms the formation of Li metal. On the contrary, Li$_x$Si/Li$_2$O composite was stable under electron beam at the same condition. The particle just shrank slightly after 1 min of exposure time, suggesting stronger binding to Li, which is consistent with the DFT simulation. Compared with core shell structure, Li$_x$Si nanodomains embedded in an Li$_2$O matrix provide a larger contact

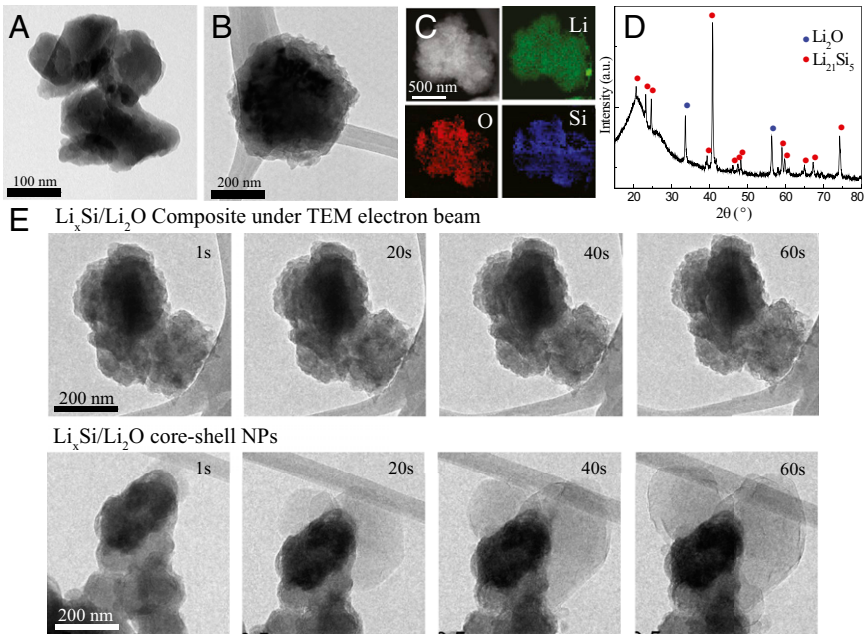

Fig. 2. Characterizations of SiO NPs before and after thermal lithiation. (*A*) TEM image of ball-milled SiO NPs. (Scale bar: 100 nm.) (*B*) TEM image of lithiated SiO NPs. (Scale bar: 200 nm.) (*C*) Scanning TEM image of lithiated SiO NPs and the corresponding EELS maps of Li, O, and Si distributions. (Scale bar: 500 nm.) (*D*) XRD pattern of lithiated SiO NPs. (*E*) The different behaviors of Li_xSi/Li_2O composite and Li_xSi/Li_2O core shell NPs under TEM electron beam with varying duration. (Scale bar: 200 nm.)

surface between Li_2O and Li_xSi, which in turn, creates more bonds between O atoms in Li_2O and Li atoms in Li_xSi.

Stability of Li_xSi/Li_2O Composites. The improved stability increases the possibility for safe handling and simplifies the requirement on the industrial battery fabrication environment. To study the stability of Li_xSi/Li_2O composite in air, the remaining capacity of the composite was tested after exposing the composites to the different air conditions with varying duration. To obtain the original capacity, lithiated SiO NPs were mixed with super P and PVDF (65:20:15 by weight) in tetrahydrofuran to form a slurry, which was then casted on copper foil. Note that slurry solvents with higher polarity should be avoided as a result of the high reactivity of Li_xSi. Half cells were fabricated by using Li metal as the counterelectrode. The cell was charged to 1.5 V at a rate of C/50, showing an extraction capacity of 2,059 mAh/g based on the mass of SiO (1 C = 2.67 A/g for SiO) (Fig. S4*A*). If calculated based on the mass of Si, the capacity was 3,236 mAh/g, close to the theoretical specific capacity of Si. The strong oxidation peak at 0.7 V in the cyclic voltammetry profile of lithiated SiO NPs (Fig. S4*B*) confirmed the formation of highly crystalline Li_xSi, consistent with the XRD result. XRD patterns of metallurgically lithiated SiO NPs in Fig. S5 show that the crystallinity of Li_xSi and Li_2O domains is improved by extending the heating time from 3 to 5 d. Usually, the stability in air increases with the degree of the crystallinity (38). Moreover, the highly crystalline Li_2O matrix would be dense enough to prevent side reactions in the air. Therefore, the sample for stability test was prepared by heating for 5 d. To test the dry air stability, Li_xSi/Li_2O composite was stored in dry air (dew point = −50 °C) with varying durations. The capacity retention is determined by charging the cell to 1.5 V. As shown in Fig. 3*A*, the Li_xSi/Li_2O composite exhibits remarkable dry air stability with negligible (9%) capacity decay after 5 d of exposure, and the trend of capacity decay is much slower compared with core shell NPs (losing 30% after 5 d).

Electrochemically lithiated Si and SiO electrodes were prepared by placing the electrolyte-wetted electrodes in direct contact with the Li metal for 24 h (Si NPs:super P:PVDF = 65:20:15 for Si electrode and SiO NPs:super P:PVDF = 65:20:15 for SiO electrode). The XRD patterns in Fig. S6 indicate that the electrochemically lithiated SiO electrode is primarily in amorphous phase, whereas lithiated Si electrode consists of crystalline $Li_{15}Si_4$ (PDF no. 01–079-5588). Surprisingly, the electrochemically lithiated Si and SiO electrodes do not exhibit dry air stability, losing most of the capacity after in dry air for just 1 d (Fig. S7). The crystallinity and phase significantly influence the stability. Amorphous phase can be treated as ultrasmall domains, which contribute to poor stability of electrochemically lithiated SiO. $Li_{21}Si_5$ is the most thermally stable phase among crystalline lithium silicides (39). Therefore, the capacity of electrochemically lithiated Si with small $Li_{15}Si_4$ domains plummeted after in dry air for 1 d. Fig. 3*B* shows the capacity retention of Li_xSi/Li_2O composites, Li_xSi/Li_2O core shell NPs, and artificial SEI-coated Li_xSi NPs in the air with different humidity levels for 6 h, from which the superior stability of the Li_xSi/Li_2O composites is evident. In our previous reports, little capacity was extracted for core shell NPs with the humidity level higher than 20% RH. Li_xSi/Li_2O composite still exhibited a high extraction capacity of 1,383 mAh/g after exposure to humid air with 20% RH (Fig. S8*B*). To further test whether Li_xSi/Li_2O composite is stable enough for the whole battery fabrication process, the remaining capacities of Li_xSi/Li_2O composite in ambient air with different durations were studied. The humidity range of the test room is from 35% to 40% RH. The TEM image (Fig. S8*A*) indicates that the morphology and surface finish remained intact after 6 h of exposure to the ambient air. Although the XRD spectrum revealed small peaks belonging to LiOH (PDF no. 00–032-0564), the intensity of Li_xSi peaks confirmed Li_xSi to remain the major component (Fig. 3*D*). Consistently, the red curve in Fig. 3*C* shows the Li_xSi/Li_2O composite with an extraction capacity of 1,240 mAh/g, indicating that the Li_xSi/Li_2O composite is potentially compatible with the industrial battery fabrication environment. DFT simulation confirms the strong binding between O atoms in Li_2O and Li in $Li_{21}Si_5$ (Fig. 1*C*). Compared with core shell structure, uniform Li_xSi/Li_2O composite exhibits larger contact surface between Li_2O and Li_xSi. Moreover, the highly crystalline Li_2O matrix formed at high temperature is dense enough to prevent side reactions in the air compared with Li_2O coating formed at room temperature. For core shell structure, any pinhole will provide a pathway for inner Li_xSi to react with the air and thus, reduce the capacity as shown in Fig. 1*B*. In Li_xSi/Li_2O

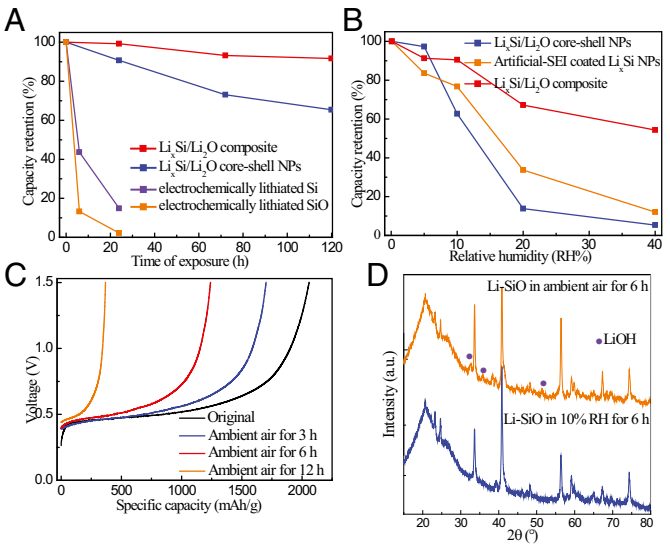

Fig. 3. Stability of Li_xSi/Li_2O composites. (*A*) Capacity retention of Li_xSi/Li_2O composites (red), Li_xSi/Li_2O core shell NPs (blue), electrochemically lithiated Si electrode (purple), and electrochemically lithiated SiO electrode (orange) exposed to dry air with varying duration. (*B*) Capacity retention of Li_xSi/Li_2O composites (red), Li_xSi/Li_2O core shell NPs (blue), and artificial SEI-coated Li_xSi NPs (orange) after 6 h of storage in the air with different humidity levels. (*C*) The remaining capacities of lithiated SiO NPs in ambient air (~40% RH) with different durations. (*D*) XRD patterns of lithiated SiO NPs exposed to ambient air for 6 h (yellow) and humid air (10% RH) for 6 h (blue).

composite, Li_xSi nanodomains are uniformly embedded in a robust Li_2O matrix, such that each Li_xSi nanodomain has localized Li_2O protection. Even if some Li_xSi nanodomains are killed because of the presence of pinholes on the surface, the inner Li_2O still serves as a localized protection layer to prevent inner Li_xSi nanodomains from additional oxidation.

Electrochemical Characteristics of Lithiated SiO NPs. Because of the sufficiently low potential, lithiated SiO NPs are readily mixed with various anode materials, such as SiO, Sn, and graphite, during slurry processing and serve as excellent prelithiation reagents. Lithiated SiO NPs were mixed with SiO, super P, and PVDF in a weight ratio of 10:55:20:15 in a slurry, which was then casted on copper foil. During the cell assembly, lithiated SiO NPs were spontaneously activated on the addition of the electrolyte, which provided additional Li ions to the anode for the partial lithiation of the SiO NPs and the formation of the SEI layer. After the cell assembly, it took about 6 h for the anode to reach equilibrium. Both the SiO cell with lithiated SiO additive and the bare SiO control cell (SiO:super P:PVDF = 65:20:15 by weight) were first lithiated to 0.01 V and then delithiated to 1 V (Fig. 4*A*). The mass includes SiO in the lithiated SiO additive. The first cycle CE of the SiO control cell was only 52.6%, because a large portion of Li was required for the reaction with SiO to form electrochemically inactive components (40). The open circuit voltage (OCV) of SiO with lithiated SiO additive is 0.35 V, much lower than that of the control cell. It suggests that lithiated SiO additive compensates for the Li consumption for SEI formation and silica conversion, and therefore, the trace directly reaches the anode lithiation voltage region. Therefore, the first cycle CE increased considerably to 93.8%. Similarly, tin NPs were also successfully prelithiated with lithiated SiO NPs, thereby improving the first cycle CE from 77.7% to 101.9% (tin:lithiated SiO = 60:5 by weight) (Fig. 4*B*). Lithiated SiO NPs were mixed with graphite and PVDF in a weight ratio of 6:84:10 to compensate for the capacity loss of graphite. Without incorporation of lithiated SiO NPs, the voltage profile of graphite control cell in Fig. 4*C* revealed an obvious plateau around 0.7 V, corresponding to the formation of an SEI layer. After prelithiation, the OCV of graphite with lithiated SiO additive decreased to 0.33 V, and the first cycle CE increases from 87.4% to 104.5%. As shown in Fig. S9, lithiated SiO exposed to ambient air for 3 h is still reactive enough to prelithiate graphite material (the same weight ratio), achieving a perfect first cycle CE of 100.1%.

Lithiated SiO NPs afford remarkable battery performance either as anode additive or anode material by itself. The cycling stability of lithiated SiO NPs was tested at C/50 for the first two cycles and C/2 for the following cycles (Fig. 4*D*). The cell capacities initially decreased because of rate change and then, increased to maintain a stable cycling performance at a high capacity of 961 mAh/g (the capacity is based on the mass of SiO.). If the capacity is based on the mass of Si, the retention capacity after 400 cycles was 1,509.5 mAh/g, more than three times the theoretical capacity of graphite. Using Li_xSi/Li_2O composite as anode material, the CE increased to 99.81% after just six cycles. Such result stands in stark contrast to previous reports, in which several hundred cycles were usually required for Si anode to reach this value (41). Moreover, in normal Si anodes, SEI rupture and reformation result in decreased CE, especially in later cycles, whereas the average CE from 200–400 cycles of Li_xSi/Li_2O composite was as high as 99.87% as indicated in the purple curve in Fig. 4*D*. There are several characteristics of the Li_xSi/Li_2O composite that enable the superior battery performance. The Li_xSi nanodomains are already in their expanded state, and sufficient space has been created during the electrode fabrication. Because of the small domain size and void space, Li_xSi will not pulverize or squeeze each other, and the Li_2O inactive phase could serve as a mechanical buffer to further alleviate the stress and volume change during cycling. In addition, unlike conventional Si anode that exposes reactive Li_xSi phase to the electrolyte, the vast majority of Li_xSi phase of the Li_xSi/Li_2O composite is enclosed in the stable Li_2O matrix. Therefore, the Li_2O inactive phase not only improves the dimensional stability but also, serves as an artificial SEI to reduce side reactions between active Li_xSi domain and electrolytes, thereby contributing to the high initial and following CEs.

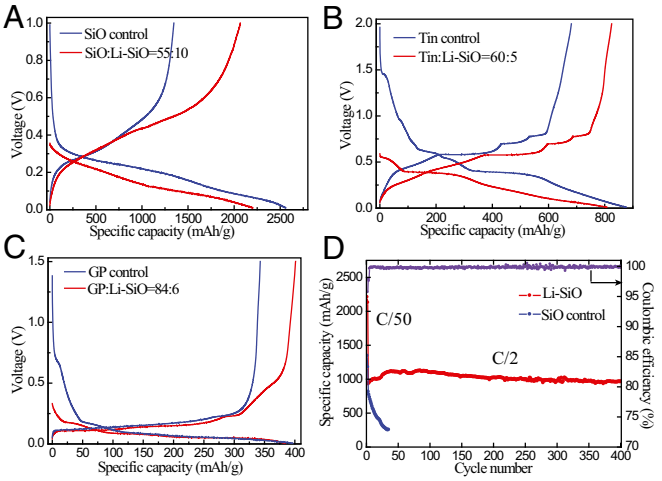

Fig. 4. Electrochemical characteristics of lithiated SiO NPs. (*A*) First cycle voltage profiles of SiO NPs:lithiated SiO composite (red; 55:10 by weight) and SiO control cell (blue) show that lithiated SiO NPs improve the first cycle CE of SiO. The capacity is based on the mass of the active materials, including SiO NPs and SiO in lithiated SiO NPs. (*B*) First cycle voltage profiles of tin:lithiated SiO composite (red; 60:5 by weight) and tin control cell (blue). The capacity is based on the mass of tin NPs and SiO in lithiated SiO NPs. (*C*) First cycle voltage profiles of graphite:lithiated SiO composite (red; 84:6 by weight) and graphite control cell (blue). The capacity is based on the mass of graphite and SiO. GP, graphite. (*D*) Cycling performance of lithiated SiO NPs and SiO control cell at C/50 for the first two cycles and C/2 for the following cycles (1 C = 2.67 A/g, and the capacity is based on the mass of SiO NPs). The purple line is the CE of lithiated SiO NPs.

Characterizations and Electrochemical Performance of Lithiated SiO_2 NPs. Previously, SiO_2 was not considered to be electrochemically active for lithium storage because of the poor electrical and ionic conductivity (42). By using fine nanostructures, SiO_2 anodes have been recently shown but with limited capacity and quick capacity decay (43). Here, we show SiO_2 as the starting material to form Li_xSi/Li_2O composite, which serves as an excellent prelithiation reagent. Sol-gel–synthesized SiO_2 NPs reacted with molten Li to form Li_xSi/Li_2O composite at the same condition. Fig. 5*A* and Fig. S10*A* show SiO_2 NPs with a narrow size distribution around 90 nm. After metallurgical lithiation, the morphology of NPs remained, whereas the size changed to 200 nm because of volume expansion (Fig. 5*B*). XRD pattern also confirms the formation of crystalline $Li_{21}Si_5$ and Li_2O during the alloying process (Fig. 5*C*). To measure the real capacity and eliminate the possible capacity loss during the slurry process, lithiated SiO_2 NPs were dispersed in cyclohexane and then, drop-casted on copper foil. The extraction capacity of lithiated SiO_2 was 1,543 mAh/g based on the mass of SiO_2 (Fig. 5*D*). The OCV of lithiated SiO_2 NPs was below 0.1 V, confirming that the majority of SiO_2 has been successfully lithiated. Similar to lithiated SiO NPs, lithiated SiO_2 NPs can undergo the slurry process with tetrahydrofuran as the slurry solvent and exhibit negligible capacity consumption. It is important to note that the galvanostatic discharge/charge profile of SiO_2 NPs (SiO_2:super P:PVDF = 65:20:15 by weight) (orange curve in Fig. 5*D*) showed little delithiation capacity after the first lithiation, indicating that the sol-gel–synthesized SiO_2 NPs are electrochemically inactive. However, thanks to the thermal lithiation process, the inactive SiO_2 NPs can be successfully converted into high-capacity anode. Because the final products of lithiated SiO and SiO_2 are the same, lithiated SiO_2 also serves as a prelithiation reagent. Similarly, lithiated SiO_2 NPs were mixed with graphite and PVDF in a weight ratio of 6:84:10 to achieve high first CE of 99.7% (Fig. S10*C*). Because of the nanoscale dimension and the small amount, prelithiation reagents tend to be embedded in the interstices of graphite microparticles. Therefore, graphite prelithiated with lithiated SiO_2 NPs follows the trend of the graphite control cell and exhibits stable cycling performance at C/5 (1 C = 372 mA/g) (Fig. S10*D*). To verify the electrochemical performance of the prelithiation reagents more effectively, $LiFePO_4$/prelithiated graphite (graphite:Li-SiO_2 = 84:6 by weight) full cells were tested in the voltage range from 2.5 to 3.8 V at C/5. The rate and cell capacity are based on the mass of $LiFePO_4$ in the cathode. After incorporating lithiated SiO_2 NPs into the graphite, the OCV of full cell before cycling is 2.5 V, and the plateau between 2.7 and 3.2 V, corresponding to the SEI formation, totally disappeared as shown in Fig. 5*E*. As a result, the first cycle CE increases from 82.4% to 94.3%. Cycling at C/5, the higher capacity of the full cell with lithiated SiO_2 NPs was preserved over all 90 cycles (Fig. 5*F*). The average CE of the full cell with lithiated SiO_2 is 99.1%, which is higher than the regular full cell (98.8%) for the same cycling period. Lithiated SiO_2 NPs effectively suppress the undesired consumption of Li from cathode materials, which in turn, increases the energy density of the full cell.

Conclusions

In summary, Li_xSi/Li_2O composites were synthesized through a one-pot metallurgical process using low-cost SiO and SiO_2 as the starting materials. The product revealed a unique structure with homogeneously dispersed active Li_xSi nanodomains embedded in a robust Li_2O matrix, which yielded the composite with unparalleled air stability and cycling performance. Other than negligible capacity decay in dry air, Li_xSi/Li_2O composites exhibited a high capacity of 1,240 mAh/g after 6 h of exposure to ambient air (~40% RH). The improved stability simplified the requirement on the industrial battery fabrication environment, which in turn, can decrease the battery manufacturing cost. As a prelithiation reagent, the Li_xSi/Li_2O composite was shown to be effective to compensate for the first cycle irreversible capacity loss for both intercalation and alloying anodes, which is generally applicable to advanced nanostructured materials with large first cycle irreversible capacity losses. Moreover, the composite is also capable of functioning as anode material, which exhibits stable cycling performance and consistently high CEs (99.81% at the seventh cycle and stable at ~99.87% for 400 cycles). Therefore, this novel Li-rich anode material has great potential to replace the dendrite-forming lithium metal anodes in next generation high-energy density batteries, such as Li-O_2 and Li-S batteries.

Materials and Methods

DFT Simulation. First principles calculations were performed within the DFT framework as implemented in the Materials Studio, version 5.5. The electron exchange and correlation interaction is described by the generalized gradient approximation method. The following valence electron configurations were used: Si ($3s^23p^3$), O ($2s^22p^4$), and Li ($2s^1$). After checking for convergence, 450 eV was chosen as the cutoff energy of the plane-wave basis for the Kohn–Sham

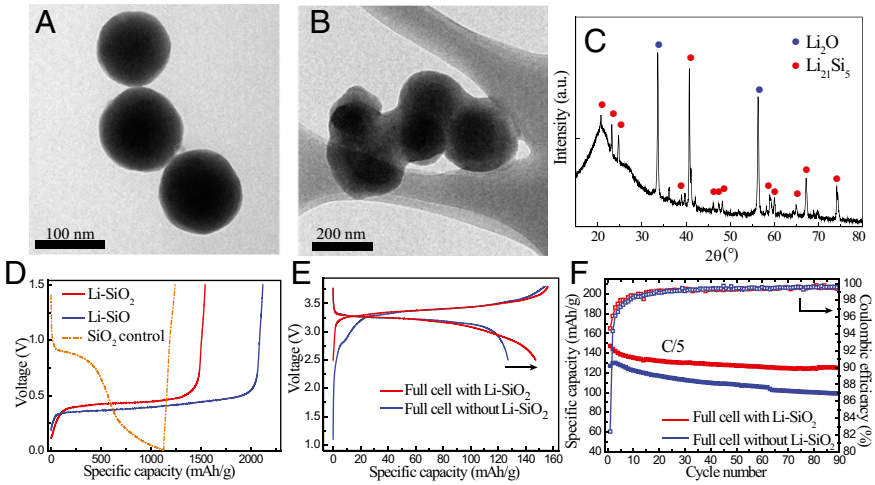

Fig. 5. Characterizations and electrochemical performance of SiO_2 NPs before and after thermal lithiation. (*A*) TEM image of sol-gel–synthesized SiO_2 NPs. (Scale bar: 100 nm.) (*B*) TEM image of lithiated SiO_2 NPs. (Scale bar: 200 nm.) (*C*) XRD pattern of lithiated SiO_2 NPs. (*D*) First cycle delithiation capacity of lithiated SiO_2 NPs (red) and SiO NPs (blue). Galvanostatic lithiation/delithiation profile of SiO_2 NPs in the first cycle is in orange. The capacity is based on the mass of SiO or SiO_2 in the anode. (*E*) First cycle voltage profiles of $LiFePO_4$/graphite full cell with (red) and without (blue) Li-SiO_2 NPs (graphite:Li-SiO_2 = 84:6 by weight). (*F*) Cycling performance and CE of full cells with (red) and without (blue) Li-SiO_2 NPs. The rate and cell capacity are both based on the mass of $LiFePO_4$ in the cathode.

states. All atomic positions and lattice vectors were fully optimized using a conjugate gradient algorithm to obtain the unstrained configuration. Atomic relaxation was performed until the change of total energy was less than 10^{-5} eV and all of the forces on each atom were smaller than 0.01 eV/Å.

Synthesis of Li_xSi/Li_2O Composites. SiO microparticles (−325 mesh; Sigma Aldrich) were ball-milled at a grinding speed of 400 rpm for 6 h. To synthesize SiO_2 NPs, ammonia hydroxide solution [1 mL NH_4OH (Fisher Scientific), 5 mL H_2O, 15 mL ethanol (Fisher Scientific)] was poured into tetraethyl orthosilicate (TEOS) solution [1 mL TEOS (99.999% trace metal basis; Sigma Aldrich), 15 mL ethanol] while stirring. The reaction was left at 55 °C under stirring at 500 rpm for 2 h. The NPs were cleaned and collected by centrifuging at 5,000 rpm three times. Both SiO and SiO_2 NPs were dried under vacuum for 48 h and then, heated to 120 °C in the glove box for 24 h. SiO or SiO_2 NPs were heated to 250 °C followed by the addition of Li metal foil (99.9%; Alfa Aesar). The ratios of SiO to Li and SiO_2 to Li were determined by the chemical equations in Fig. S1. The mixture was heated at 250 °C under mechanical stir at 200 rpm for at least 1 d in an Ar glove box (H_2O level < 0.1 ppm and O_2 level < 1.2 ppm).

Characterizations. Powder XRD patterns were obtained on a PANalytical X'Pert Diffractometer with Ni-filtered Cu Kα radiation. SEM and TEM images were taken using an FEI XL30 Sirion SEM and an FEI Tecnai G^2 F20 X-Twin Microscope, respectively. TEM videos were also taken on a Tecnai Microscope with a magnification of 13,500× and a spot size of five. Compositional analysis was obtained by EELS mapping collection using an FEI Titan 80–300 Environmental TEM at an acceleration voltage of 300 kV. The energy resolution of the EELS spectrometer was 0.8 eV as measured by the full width at half magnitude of the zero loss peak. EELS mapping data were acquired using a C2 aperture size of 50 mm and a camera length of 60 mm. To obtain the range of Li, Si, and O at the same particle, the dual detector was used with different acquisition times of 0.2 and 2 s for low- and high-loss range, respectively. The energy windows of the EELS were 40–145 eV for Li (Li-K edge, 54.7 eV) and Si (Si-L2, 3 edge, 99.2 eV) peaks and 510–615 eV for O (O-K edge, 532 eV) peak. Mapping images were collected after extracting the peaks of Li-K, Si-L, and O-K edges at 54.7, 99.2, and 532 eV, respectively.

Electrochemical Measurements. Cyclic voltammetry measurements were performed on a BioLogic VMP3 System. Galvanostatic cycling was performed using a 96-channel battery tester (Arbin Instrument). To prepare the working electrodes, anode materials were dispersed uniformly in tetrahydrofuran (Sigma Aldrich) to form a slurry, which was then casted onto a copper foil. The mass loading of Li_xSi/Li_2O composite-based cells was 0.8–1.5 mg/cm^2, and the mass loading of graphite-based cells was 2.0–3.0 mg/cm^2. The electrolyte was 1.0 M $LiPF_6$ in 1:1 (wt/wt) ethylene carbonate/diethyl carbonate (BASF).

ACKNOWLEDGMENTS. We acknowledge support from the Assistant Secretary for Energy Efficiency and Renewable Energy, Office of Vehicle Technologies, Battery Materials Research Program of the US Department of Energy.

1. Goodenough JB, Manthira A (2014) A perspective on electrical energy storage. *MRS Commun* 4(4):135–142.
2. Chu S, Majumdar A (2012) Opportunities and challenges for a sustainable energy future. *Nature* 488(7411):294–303.
3. Choi NS, et al. (2012) Challenges facing lithium batteries and electrical double-layer capacitors. *Angew Chem Int Ed Engl* 51(40):9994–10024.
4. Tarascon JM, Armand M (2001) Issues and challenges facing rechargeable lithium batteries. *Nature* 414(6861):359–367.
5. Xu K (2014) Electrolytes and interphases in Li-ion batteries and beyond. *Chem Rev* 114(23):11503–11618.
6. Palacín MR, de Guibert A (2016) Why do batteries fail? *Science* 351(6273):1253292.
7. Xu K (2004) Nonaqueous liquid electrolytes for lithium-based rechargeable batteries. *Chem Rev* 104(10):4303–4417.
8. Yoshio M, Wang HY, Fukuda K, Hara Y, Adachi Y (2000) Effect of carbon coating on electrochemical performance of treated natural graphite as lithium-ion battery anode material. *J Electrochem Soc* 147(4):1245–1250.
9. Ohzuku T, Iwakoshi Y, Sawai K (1993) Formation of lithium-graphite intercalation compounds in nonaqueous electrolytes and their application as a negative electrode for a lithium ion (shuttlecock) cell. *J Electrochem Soc* 140(9):2490–2498.
10. Zhao H, Yuan W, Liu G (2015) Hierarchical electrode design of high-capacity alloy nanomaterials for lithium-ion batteries. *Nano Today* 10(2):193–212.
11. Su X, et al. (2014) Silicon-based nanomaterials for lithium-ion batteries: A Review. *Adv Energy Mater* 4(1):1300882–1300905.
12. McDowell MT, Lee SW, Nix WD, Cui Y (2013) 25th Anniversary article: Understanding the lithiation of silicon and other alloying anodes for lithium-ion batteries. *Adv Mater* 25(36):4966–4985.
13. Jeong S, et al. (2013) Etched graphite with internally grown Si nanowires from pores as an anode for high density Li-ion batteries. *Nano Lett* 13(7):3403–3407.
14. Luo L, et al. (2015) Surface-coating regulated lithiation kinetics and degradation in silicon nanowires for lithium ion battery. *ACS Nano* 9(5):5559–5566.
15. Chan CK, et al. (2008) High-performance lithium battery anodes using silicon nanowires. *Nat Nanotechnol* 3(1):31–35.
16. Liu N, Huo K, McDowell MT, Zhao J, Cui Y (2013) Rice husks as a sustainable source of nanostructured silicon for high performance Li-ion battery anodes. *Sci Rep* 3:1919.
17. Li X, et al. (2014) Mesoporous silicon sponge as an anti-pulverization structure for high-performance lithium-ion battery anodes. *Nat Commun* 5:4105.
18. Son IH, et al. (2015) Silicon carbide-free graphene growth on silicon for lithium-ion battery with high volumetric energy density. *Nat Commun* 6:7393.
19. Yamada M, Ueda A, Matsumoto K, Ohzuku T (2011) Silicon-based negative electrode for high-capacity lithium-ion batteries: "SiO"-carbon composite. *J Electrochem Soc* 158(4):417–421.
20. Zamfir MR, Nguyen HT, Moyen E, Lee YH, Pribat D (2013) Silicon nanowires for Li-based battery anodes: A review. *J Mater Chem A* 1(34):9566–9586.
21. Wu H, Cui Y (2012) Designing nanostructured Si anodes for high energy lithium ion batteries. *Nano Today* 7(5):414–429.
22. Zheng H, Li J, Song X, Liu G, Battaglia VS (2012) A comprehensive understanding of electrode thickness effects on the electrochemical performances of Li-ion battery cathodes. *Electrochim Acta* 71(1):258–265.
23. Obrovac MN, Chevrier VL (2014) Alloy negative electrodes for Li-ion batteries. *Chem Rev* 114(23):11444–11502.
24. Moorhead-Rosenberg Z, Allcorn E, Manthiram A (2014) In situ mitigation of first-cycle anode irreversibility in a new spinel/FeSb lithium-ion cell enabled via a microwave-assisted chemical lithiation process. *Chem Mater* 26(20):5905–5913.
25. Tarascon JM, Guyomard D (1991) Li metal-free rechargeable batteries based on $Li_{1+X}Mn_2O_4$ cathodes and carbon anodes. *J Electrochem Soc* 138(10):2864–2868.
26. Sun Y, et al. (2016) High-capacity battery cathode prelithiation to offset initial lithium loss. *Nat Energy* 1:15008.
27. Seh ZW, et al. (2014) Two-dimensional layered transition metal disulphides for effective encapsulation of high-capacity lithium sulphide cathodes. *Nat Commun* 5:5017.
28. Wang C, et al. (2015) Slurryless Li_2S/reduced graphene oxide cathode paper for high-performance lithium sulfur battery. *Nano Lett* 15(3):1796–1802.
29. Kim HJ, et al. (2016) Controlled prelithiation of silicon monoxide for high performance lithium-ion rechargeable full cells. *Nano Lett* 16(1):282–288.
30. Hassoun J, et al. (2012) A contribution to the progress of high energy batteries: A metal-free, lithium-ion, silicon-sulfur battery. *J Power Sources* 202:308–313.
31. Wang ZH, et al. (2014) Application of stabilized lithium metal powder (SLMP (R)) in graphite anode—a high efficient prelithiation method for lithium-ion batteries. *J Power Sources* 260:57–61.
32. Zhao H, et al. (2014) Toward practical application of functional conductive polymer binder for a high-energy lithium-ion battery design. *Nano Lett* 14(11):6704–6710.
33. Forney MW, Ganter MJ, Staub JW, Ridgley RD, Landi BJ (2013) Prelithiation of silicon-carbon nanotube anodes for lithium ion batteries by stabilized lithium metal powder (SLMP). *Nano Lett* 13(9):4158–4163.
34. Wang L, Fu YB, Battaglia VS, Liu G (2013) SBR-PVDF based binder for the application of SLMP in graphite anodes. *RSC Adv* 3(35):15022–15027.
35. Zhao J, et al. (2014) Dry-air-stable lithium silicide-lithium oxide core-shell nanoparticles as high-capacity prelithiation reagents. *Nat Commun* 5:5088.
36. Zhao J, et al. (2015) Artificial solid electrolyte interphase-protected Li_xSi nanoparticles: An efficient and stable prelithiation reagent for lithium-ion batteries. *J Am Chem Soc* 137(26):8372–8375.
37. Hassoun J, et al. (2012) A metal-free, lithium-ion oxygen battery: A step forward to safety in lithium-air batteries. *Nano Lett* 12(11):5775–5779.
38. Xu CN, Tamaki J, Miura N, Yamazoe N (1991) Grain-size effects on gas sensitivity of porous SnO_2-based elements. *Sens Actuators B Chem* 3(2):147–155.
39. Wang CM, et al. (2012) In situ TEM investigation of congruent phase transition and structural evolution of nanostructured silicon/carbon anode for lithium ion batteries. *Nano Lett* 12(3):1624–1632.
40. Park E, et al. (2015) Dual-size silicon nanocrystal-embedded SiO_x nanocomposite as a high-capacity lithium storage material. *ACS Nano* 9(7):7690–7696.
41. Liu N, et al. (2014) A pomegranate-inspired nanoscale design for large-volume-change lithium battery anodes. *Nat Nanotechnol* 9(3):187–192.
42. Chang WS, et al. (2012) Quartz (SiO_2): A new energy storage anode material for Li-ion batteries. *Energy Environ Sci* 5(5):6895–6899.
43. Yan N, et al. (2013) Hollow porous SiO_2 nanocubes towards high-performance anodes for lithium-ion batteries. *Sci Rep* 3:1568.

Supporting Information

Zhao et al. 10.1073/pnas.1603810113

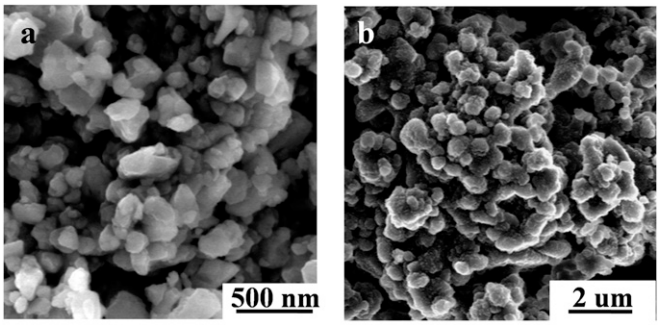

Fig. S1. SEM images of (*A*) ball-milled SiO NPs and (*B*) thermal lithiated SiO NPs. The chemical equations of thermal lithiation of (*C*) SiO and (*D*) SiO_2.

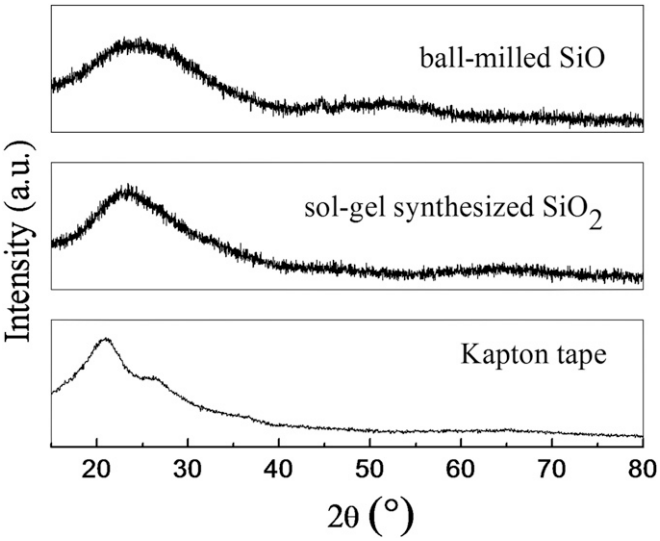

Fig. S2. XRD patterns of (*Top*) ball-milled SiO NPs, (*Middle*) sol-gel–synthesized SiO_2 NPs, and (*Bottom*) Kapton tape.

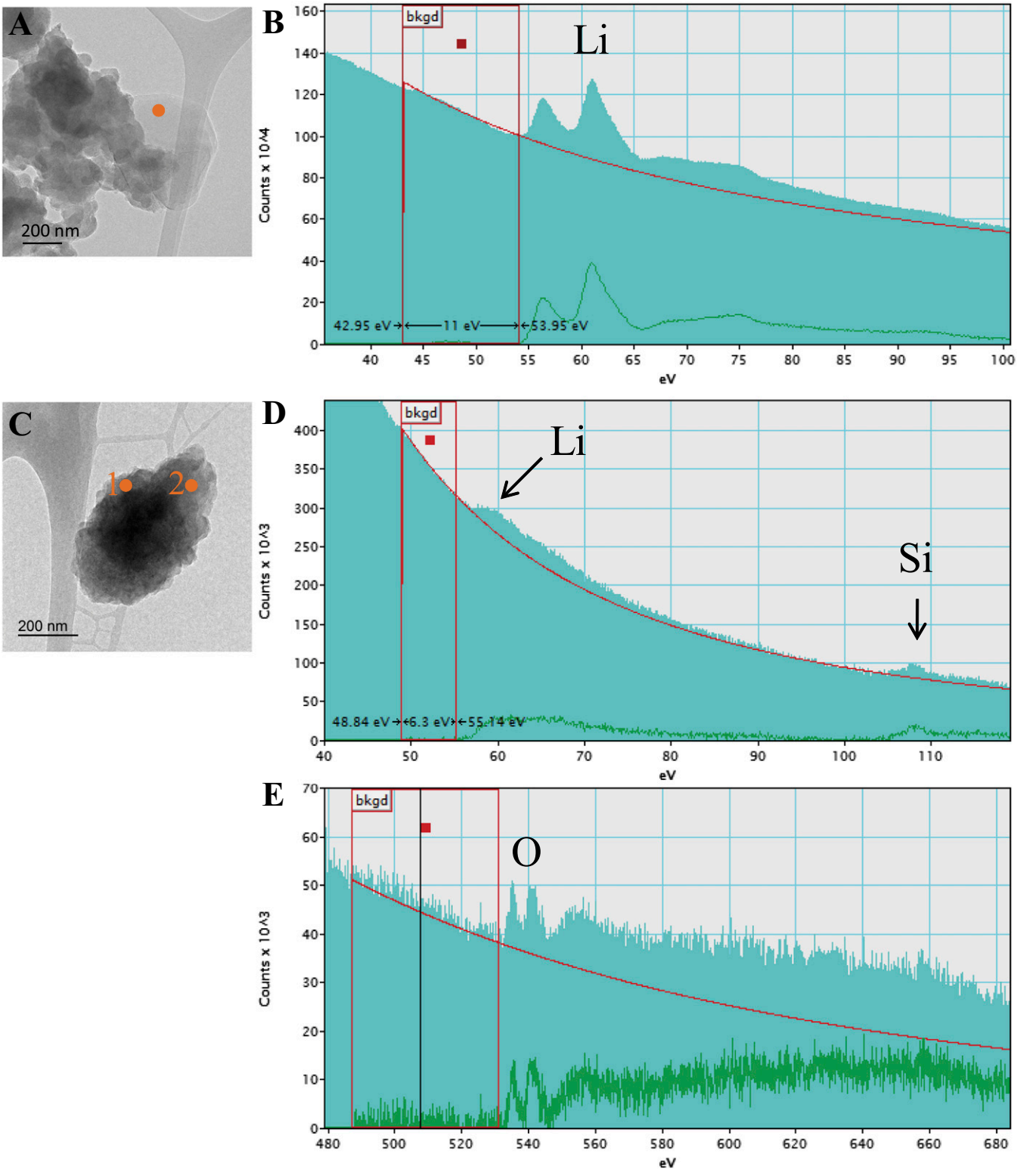

Fig. S3. (*A*) TEM image of Li_xSi/Li_2O core shell NPs under TEM electron beam for 30 s. (*B*) The EELS spectrum collected at the orange spot marked in *A* confirms the formation of Li metal. (*C*) TEM image of Li_xSi/Li_2O composite under TEM electron beam for 30 s. (*D*) EELS spectrum of Li and Si collected at orange spot 1 marked in *C*. (*E*) EELS spectrum of O collected at orange spot 2 marked in *C*.

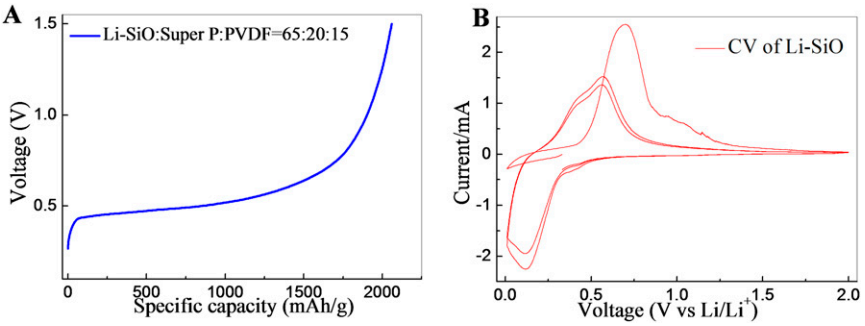

Fig. S4. (*A*) First cycle delithiation capacity of the lithiated SiO NPs (Li-SiO NPs:super P:PVDF = 65:20:15 by weight). (*B*) Cyclic voltammetry measurement of lithiated SiO NPs at a scan rate of 0.1 mV s^{-1} over the potential window from 0.01 to 2 V vs. Li/Li^+. CV, cyclic voltammetry.

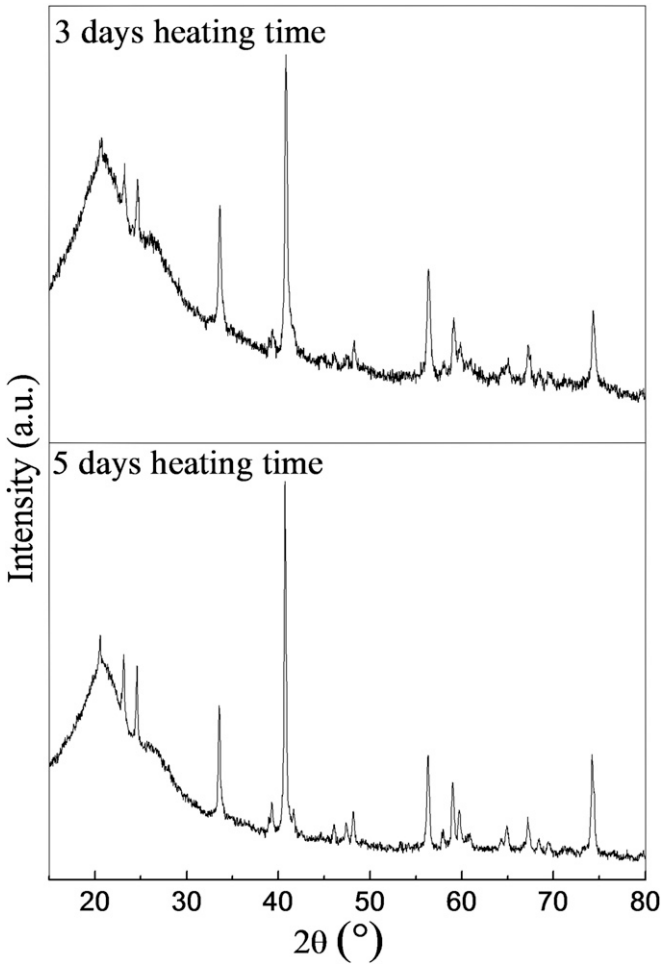

Fig. S5. XRD patterns of thermal lithiated SiO NPs with heating times of (*Upper*) 3 and (*Lower*) 5 d.

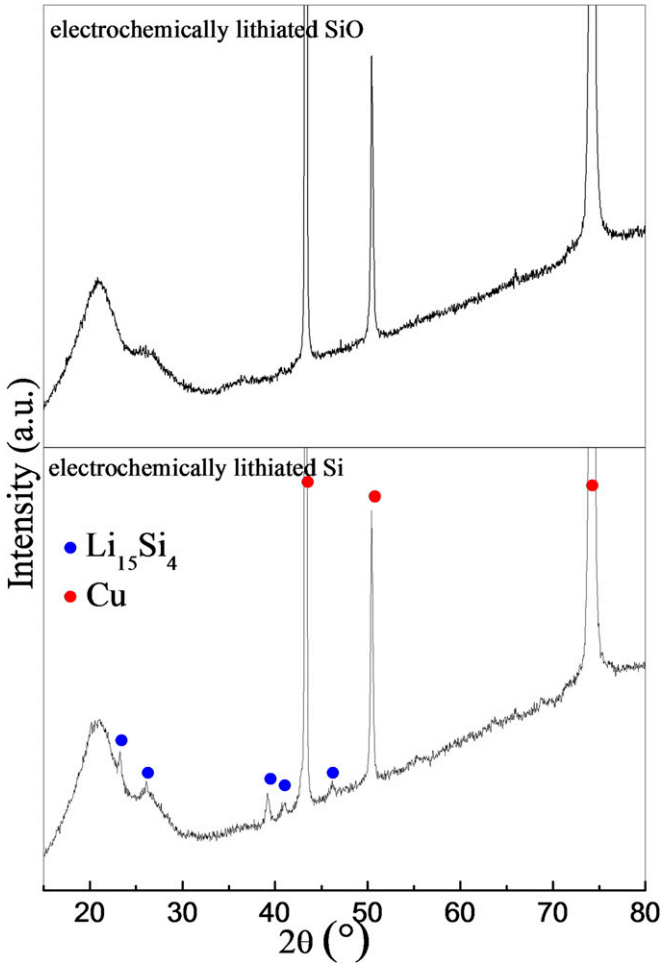

Fig. S6. XRD patterns of (*Upper*) electrochemically lithiated SiO electrode and (*Lower*) electrochemically lithiated Si electrode.

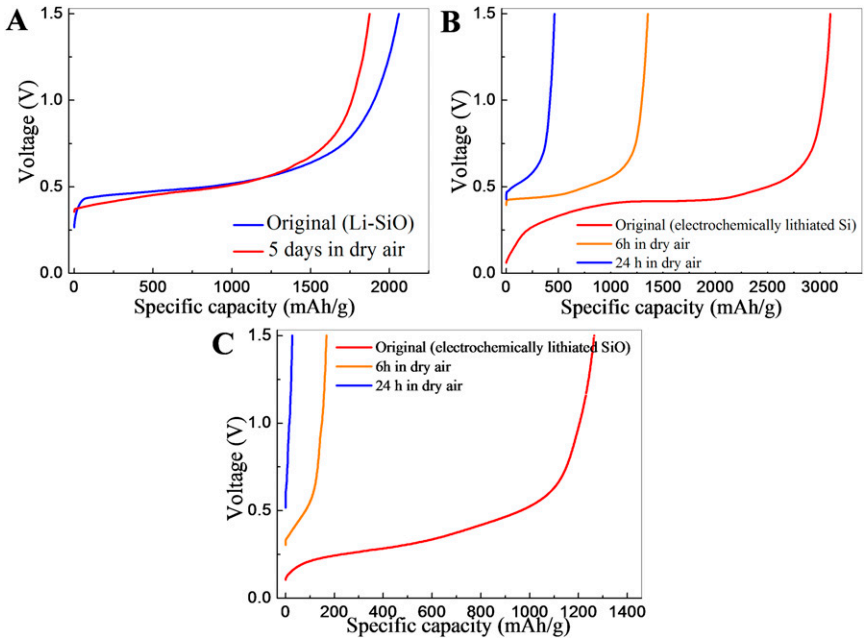

Fig. S7. The remaining capacities of (*A*) lithiated SiO NPs, (*B*) electrochemically lithiated Si NPs electrode, and (*C*) electrochemically lithiated SiO NPs electrode exposed to dry air with varying duration.

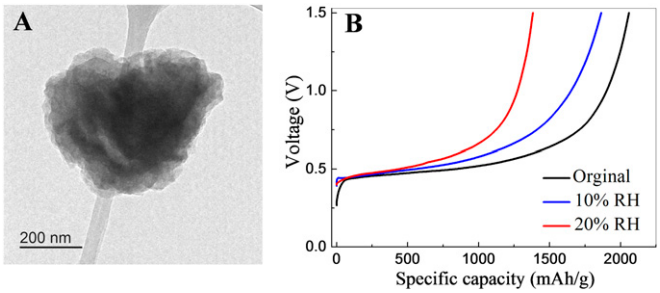

Fig. S8. (*A*) TEM image of lithiated SiO NPs exposed to ambient air for 6 h. (*B*) First cycle delithiation capacities of lithiated SiO NPs exposed to air for 6 h at different humidity levels.

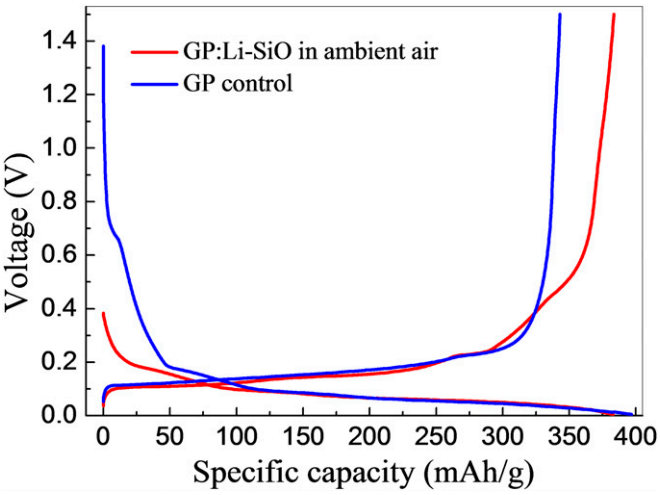

Fig. S9. First cycle voltage profile of graphite (GP) added with lithiated SiO NPs exposed to ambient air for 3 h (84:6 by weight).

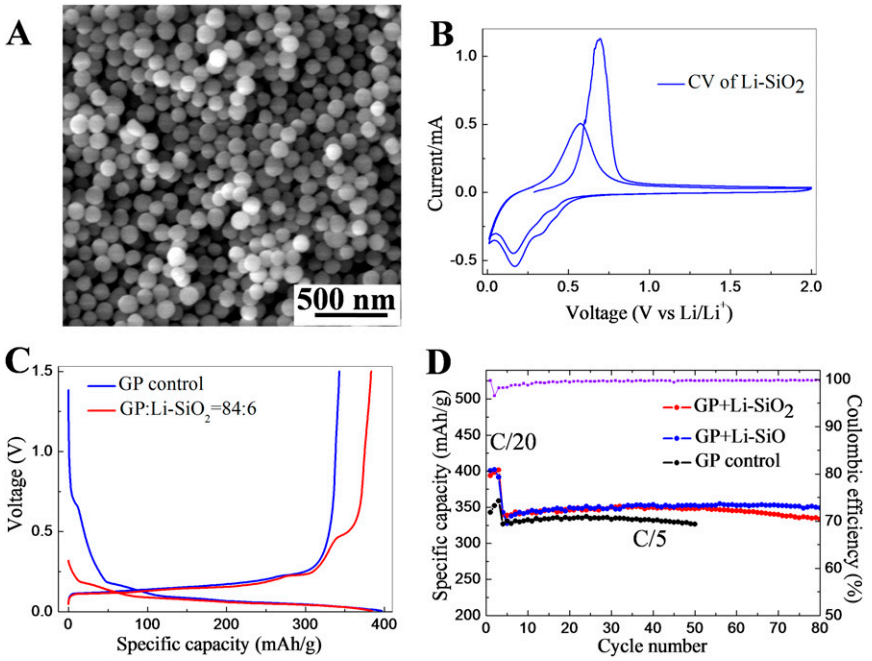

Fig. S10. (*A*) SEM image of sol-gel–synthesized SiO_2 NPs. (*B*) Cyclic voltammetry measurement of lithiated SiO_2 NPs at a scan rate of 0.1 mV s^{-1} over the potential window from 0.01 to 2 V vs. Li/Li^+. (*C*) First cycle voltage profiles of graphite:lithiated SiO_2 composite (red; 84:6 by weight) and graphite control cell (blue). (*D*) Cycling performance of graphite:lithiated SiO_2 composite (red; 84:6 by weight), graphite:lithiated SiO composite (blue; 84:6 by weight), and graphite control cell (black) at C/20 for the first three cycles and C/5 for the following cycles (1 C = 0.372 A/g C; the capacity is based on the mass of the active materials, including graphite, SiO, and SiO_2 in Li_xSi/Li_2O composites). The purple line is the CE of graphite/lithiated SiO_2 composite. CV, cyclic voltammetry; GP, graphite.

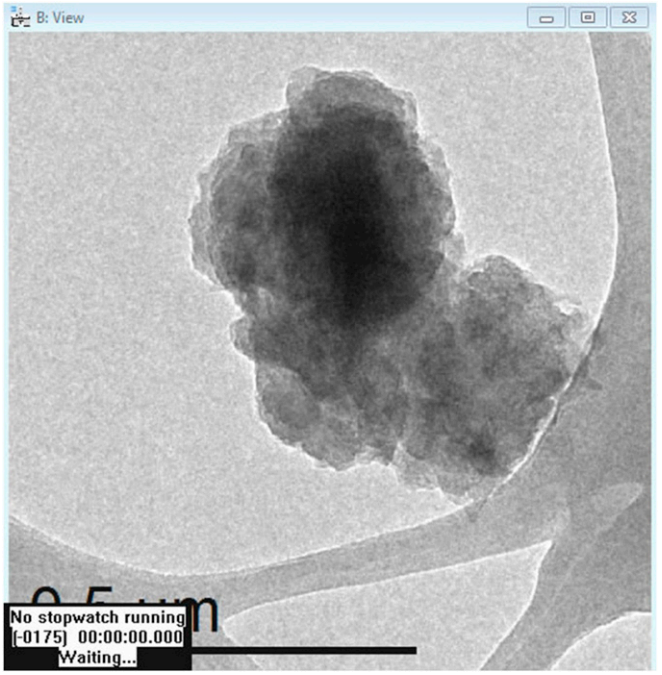

Movie S1. The behavior of Li_xSi/Li_2O composite under TEM electron beam for 1 min. The video is played at actual speed.

Movie S1

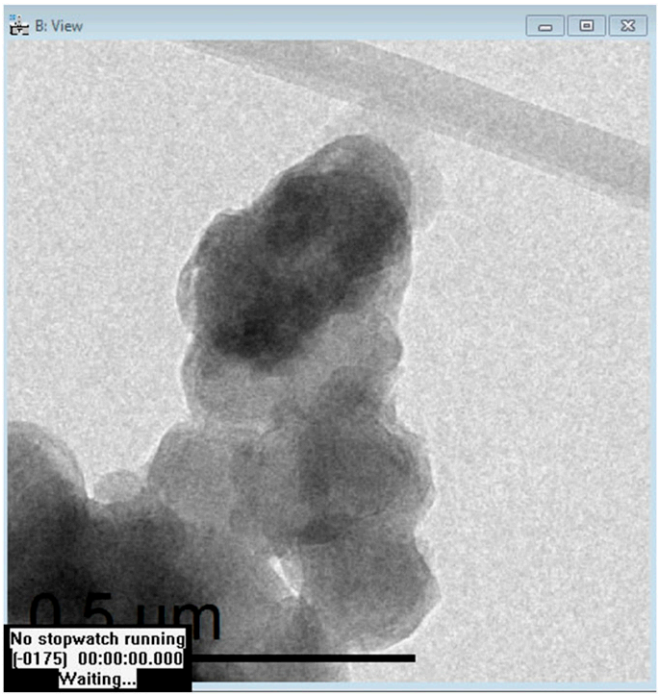

Movie S2. The behavior of Li_xSi/Li_2O core shell NPs under TEM electron beam for 1 min. The video is played at actual speed.

Movie S2